

Multifunctional Graphene-Oxide-Reinforced Dissolvable Polymeric Microneedles for Transdermal Drug Delivery

Yongli Chen,^{†,‡,||} Yikun Yang,[§] Yiwen Xian,[‡] Parbeen Singh,^{†,‡,||} Jinglong Feng,^{†,‡} Shufen Cui,[‡] Andrew Carrier,[⊥] Ken Oakes,[¶] Tiangang Luan,^{||,ID} and Xu Zhang^{*,⊥,ID}

[†]Postdoctoral Innovation Practice Base and [‡]Department of Biological Applied Engineering, Shenzhen Key Laboratory of Fermentation Purification and Analysis, Shenzhen Polytechnic, Shenzhen 518055, China

[§]National Cancer Center/National Clinical Research Center for Cancer/Cancer Hospital & Shenzhen Hospital, Chinese Academy of Medical Sciences and Peking Union Medical College, Shenzhen 518116, China

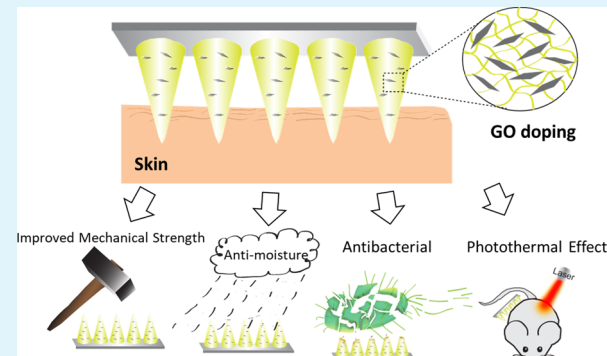
^{||}MOE Key Laboratory of Aquatic Product Safety, School of Marine Sciences, Sun Yat-sen University, Guangzhou 510275, China

[⊥]Department of Chemistry and [¶]Department of Biology, Cape Breton University, 1250 Grand Lake Road, Sydney, Nova Scotia B1P 6L2, Canada

S Supporting Information

ABSTRACT: Dissolvable polymeric microneedles (DPMNs) are promising transdermal drug delivery systems with minimal invasiveness and improved patient compliance. Incorporation of a small amount of graphene oxide (GO) in the biocompatible polymers for microneedle fabrication results in important new DPMN properties, that is, dramatically enhanced mechanic strength (10–17 times at 500 mg/mL GO), improved moisture resistance, self-sterilization, antibacterial and anti-inflammatory properties (demonstrated *in vitro*), and near-infrared light-activated controlled drug release (demonstrated *in vitro* and *in vivo*), which were exploited for the transdermal delivery of the chemotherapeutic, HA15, to melanoma-bearing mouse models. These new properties improve their efficacy of transdermal drug delivery and ease of use, enhance their capability of controlled drug release, enlarge the scope of the polymers that can be used for DPMN fabrication, prevent microbial contamination during storage and transportation, and reduce infection risk in clinical applications.

KEYWORDS: *polymeric microneedles, transdermal drug delivery, graphene oxide, mechanic strength, self-sterilizing, photothermal effect*



1. INTRODUCTION

Dissolvable polymeric microneedles (DPMNs) are arrays of miniaturized needles with a height of <1 mm. They painlessly penetrate the stratum corneum and deliver a therapeutic cargo into the dermis or onward into systemic circulation via diffusion.¹ DPMNs have been studied over the last 20 years because they are an effective transdermal drug delivery system with minimal invasiveness,^{2,3} whose excellent patient compliance and ease of self-administration are among their most attractive attributes. The bioactivity of matrix-encapsulated macromolecules, such as proteinaceous enzymes and hormones, is well preserved under ambient storage conditions,^{4–7} which facilitates their distribution, for example, for vaccine delivery.^{8,9} This is attractive in remote and resource-limited areas where cold storage and transportation are unavailable. In contrast to using reusable stainless-steel hypodermic needles (HDNs), using DPMNs also eliminates the generation of hazardous sharp wastes and thus the chance of injury and

transmission of blood-borne infections, such as HIV, hepatitis, and so on.

However, technical challenges limit their clinical application potential. Prausnitz et al.⁴ identified three material requirements for DPMN fabrication: mechanical strength to pierce the stratum corneum, biocompatibility with minimal side effects, and controlled drug release capability. Microbial contamination and infections at microneedle (MN) puncture sites must also be considered.¹⁰ Donnelly et al. demonstrated that the micropores produced by MN insertion act as entry channels for microbes to enter the dermis and cause infections.¹¹ This risk is lower than when using HDNs because of the smaller size and depth of the pores, but the large number of pores generated and high bacterial adherence to biocompatible MN polymers, for example, polysaccharides,

Received: October 29, 2019

Accepted: December 11, 2019

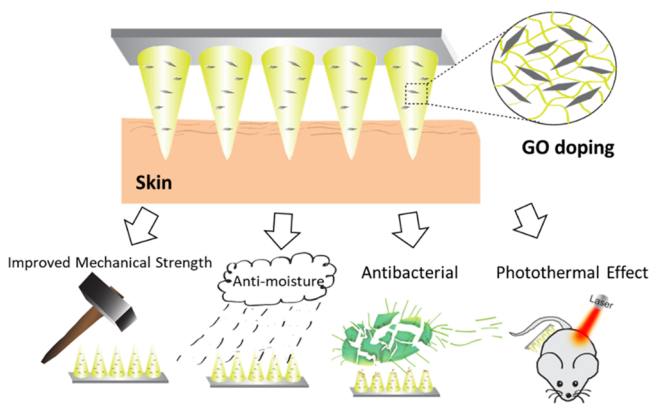
Published: December 11, 2019

compared to stainless-steel HDNs, may cause microbial infections. Microbial contamination can occur during manufacturing, packaging, transportation, and/or storage, so apart from causing infections in patients, the bacteria can also decompose therapeutics and produce toxins. Therefore, self-sterilizing DPMNs are desirable.¹²

To date, various innovative materials, including polymers and composite materials, have been investigated;^{8,13–15} for example, incorporation of 1–2% reduced graphene oxide (rGO),¹⁶ magnetic graphene quantum dots (MGQDs),¹⁷ graphene quantum dots (GQDs),¹⁸ or graphene¹⁹ in polymers for DPMN fabrication provided new properties, such as improved mechanical strength and enhanced release of macromolecular therapeutics by electrical stimulation. However, the antibacterial properties of GO^{20,21} and their photothermal effects for controlled drug release^{22,23} have never been explored for DPMN applications beyond in vitro evaluation of direct photothermal killing of cancer cells in microplate wells.¹⁹ In addition, the clinical benefits resulting from the excellent mechanical properties (ductility and stiffness)^{24,25} of GO have not been fully demonstrated.

Herein, we found that many aforementioned challenges can be addressed simply by incorporation of ≤ 0.5 wt % GO in the DPMN formulations (Scheme 1). Combining both in vitro and

Scheme 1. Graphene Oxide-Reinforced Polymeric Microneedles



in vivo tests, this study demonstrates important novel functions that GO endows to DPMNs, including improved moisture resistance, antibacterial and anti-inflammatory effects, photo-activatable drug release, and enhanced mechanical strength, leading to a broadened scope of polymers for microneedle fabrication and multiple clinical benefits.

2. RESULTS AND DISCUSSION

Our MN patches are fabricated through micromolding because it is simple, straightforward, scalable, and cost-effective. By using a male master template array made through 3D printing, we fabricated poly(dimethylsiloxane) (PDMS) female molds based on the established method.²⁶ PDMS was used to produce the female molds because of its ease of use, low cost, biocompatibility, chemical inertness (which allows for reusability), mechanical flexibility, durability, and low adhesion (which facilitates MN removal without damaging their microstructure).^{4,27,28} The female molds faithfully transferred the shape, that is, 10 \times 10 square pyramidal MNs, and geometry, that is, 350 μm base width, 700 μm height, $\sim 15 \mu\text{m}$

tip width, and 500 μm needle center-to-center spacing, to the final DPMNs. Herein, three representative biocompatible polymers, poly(vinylpyrrolidone) (PVP, MW = 30,000 Da), carboxymethyl cellulose (CMC, MW = 250,000 Da), and sodium hyaluronate (HA, MW = 200,000–300,000 Da), were selected to form the GO-doped polymeric MN patches.

The female molds were exposed to a brief oxygen plasma treatment to increase their surface hydrophilicity to facilitate the introduction of aqueous polymer solutions, which formed the MN patch after treatment at 40 °C for 12 h (Scheme S1). The MNs were gently peeled away from the mold with adhesive tape and stored in a desiccator before use. The MN patches were highly uniform in geometry (Figure 1 and Figures

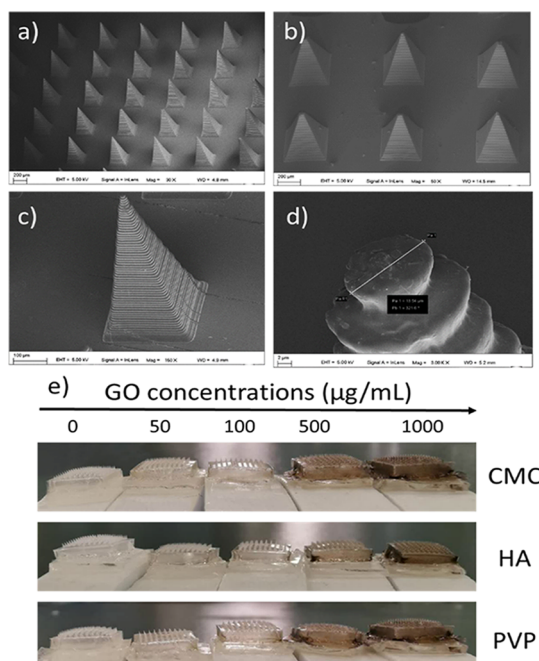


Figure 1. SEM images of the uniformly distributed PVP MNs with direct magnification of (a) 30, (b) 50, (c) 150, and (d) 3000 times. (e) Digital images of CMC, HA, and PVP MNs containing different GO concentrations.

S1 and S2) and chemical composition, which was demonstrated by the homogeneous distribution of GO throughout the polymer matrices as characterized by Raman spectroscopy (Figures S3–S5) and scanning electron microscopy (Figure S6).

The GO-doped DPMNs had five important advantages. First, their mechanical strength was greatly enhanced, as illustrated by their force–displacement curves (Figure 2 and Figure S7). As shown in Figure 2b, all three DPMNs have increasing mechanical strength with increasing GO concentration up to 500 $\mu\text{g}/\text{mL}$ (17, 15, and 10 times for HA, CMC, and PVP DPMNs, respectively), which subsequently decreased up to 1000 $\mu\text{g}/\text{mL}$, presumably because of the formation of GO aggregates within the matrix.^{29,30} Second, GO doping reduces hygroscopicity without changing their dissolution kinetics in the interstitial fluid within the skin (Figure S8). Third, the GO-doped DPMNs are inherently self-sterilizing. Fourth, GO gives the DPMNs photothermal activity,³¹ which can exploit near infrared (NIR) irradiation for controlled drug release. Finally, the GO does not adversely affect their biocompatibility.

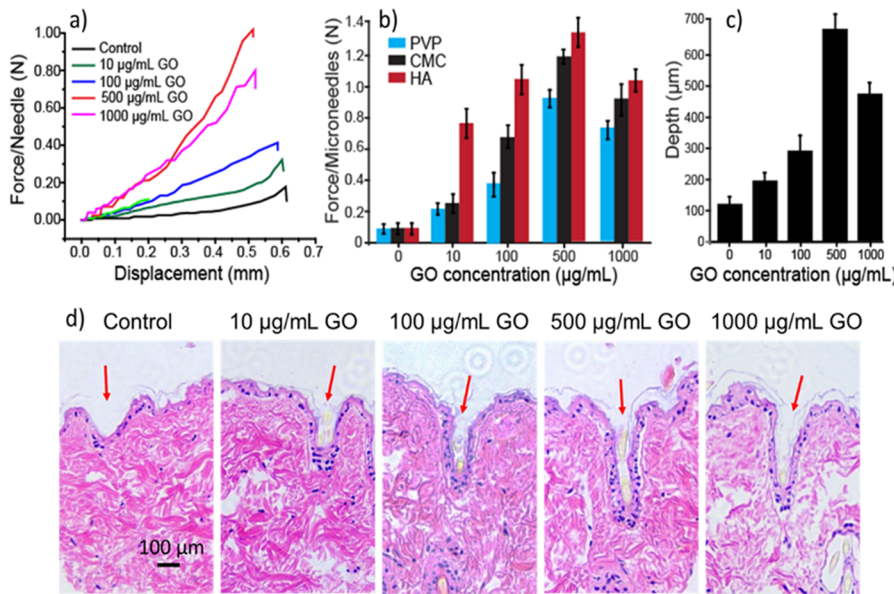


Figure 2. (a) Mechanical behaviors of PVP microneedles (MNs) and (b) MNs made of PVP, CMC, and HA with different GO concentrations ($n = 3$). (c) Skin insertion depth of PVP MNs containing different concentrations of GO ($n = 3$). (d) Microscope images of skin cross sections after PVP MN treatment. The red arrows indicate MN insertion points.

Prior work demonstrates the failure or incompleteness of skin penetration for DPMNs because of the elasticity and deformation of skin,^{32,33} which results in inaccurate or unsuccessful drug administration. Therefore, increased DPMN mechanical strength provides clinical benefit. The inclusion of GO, the strongest manmade material, reinforces mechanical strength, as widely demonstrated in materials engineering studies.^{16–19,34,35} We observed complete insertion (98–100%) of PVP MNs by incorporating 500 µg/mL GO, which improved their insertion depth 6 times relative to GO-free PVP DPMNs (Figure 2c,d). GO incorporation increased the scope of viable polymers; for example, CMC (MW = 90,000 Da) (failure force, 0.04 N) has insufficient mechanical strength for transdermal applications (threshold, 0.15 N).^{36,37} However, GO (500 µg/mL) significantly reinforced the CMC, increasing its failure force 5 times, up to ~0.2 N (Figure S9). Expanding the scope of acceptable polymers for MN fabrication allows for new functional polymers to be explored and makes more therapeutics suitable for DPMN delivery.

DPMNs, such as those made from polysaccharides, are inherently hygroscopic and deliquescent, which facilitates rapid drug release; however, this can result in softening or blunting of their tips if exposed to humid air for too long before application, which may prevent skin penetration. However, the GO–PVP DPMNs better maintained their shape and mechanical strength relative to undoped PVP, that is, a decrease in failure force from 1.0 to 0.6 N relative to ~0.18 to ~0.05 N, for GO-doped and undoped PVP DPMNs, respectively, after storage for 15 min in a humidifier (Figure 3). The moisture tolerance of GO–PVP DPMNs was presumably because of the rigid GO framework within the matrix.

Self-sterile DPMNs are critical to prevent microbial contamination and insertion site infections. As shown in Figure 4 and Figure S10, the growth of both Gram-positive bacteria *Staphylococcus aureus* (SA, ATCC 6538D-5) and Gram-negative *Escherichia coli* (EC, ATCC 8739D-5) were suppressed after interacting with GO-doped DPMNs although

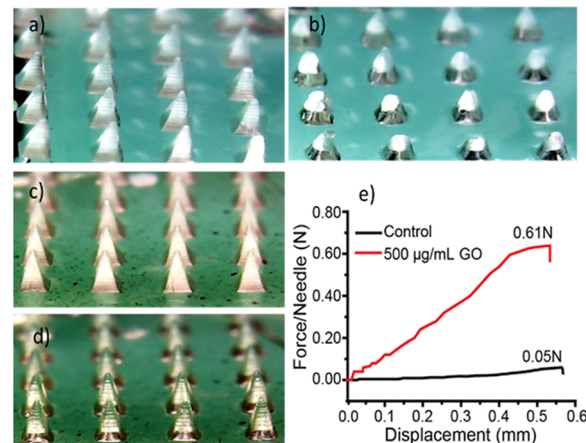


Figure 3. Moisture resistance of GO-loaded microneedles (MNs). Digital images of PVP MNs in a moist environment after (a) 0 and (b) 180 min and GO-loaded PVP MNs after (c) 0 and (d) 180 min. (e) Mechanical behaviors of PVP MNs and GO-doped PVP MNs after 15 min of exposure to humid air.

the inhibition effect for HA and CMC was less potent (i.e., 58.3 and 53.3%, respectively) than that of PVP (i.e., 95.8%) at GO concentrations of 500–1000 µg/mL. Growth inhibition is GO dose-dependent, indicating that the antibacterial effect comes from GO rather than the polymers. Additionally, we found GO effectively prevented DPMN contamination by airborne fungal spores. DPMNs were exposed to air for 3 days before cultivation in agar plates for 5 days at 37 °C, and no mold colonies were observed on plates containing DPMNs with 500–1000 µg/mL GO (Figure S10), in contrast to the large amount of mold grown on plates containing DPMNs with only 10–100 µg/mL GO. Sufficient GO loading is critical in preventing microbial contamination, which is consistent with established knowledge of the antibacterial and antifungal effect of GO, resulting from the mechanical damage of cell membranes by basal plane contact and oxidative chemical species generated at GO edges.^{38–40} This mechanism has two

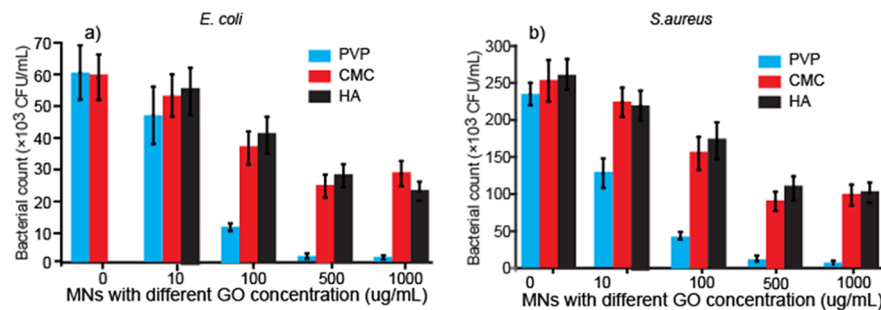


Figure 4. Quantitative analysis of colony-forming units (CFUs) with different microneedles (MNs). CFUs of (a) *E. coli* and (b) *S. aureus* with PVP, CMC, and HA MNs containing different concentrations of GO ($n = 3$).

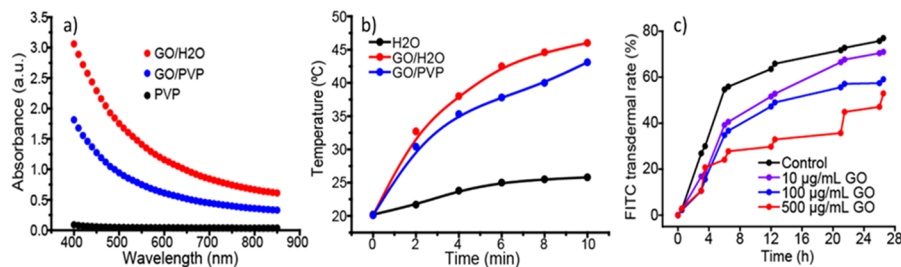


Figure 5. (a) Light absorbance spectra of PVP, GO, and GO/PVP solution. (b) Temperature increase of pure water and aqueous solutions of GO and GO/PVP irradiated with an 850 nm laser. (c) In vitro transdermal permeation kinetics of FITC (a model pharmaceutical) in GO-doped PVP microneedles through mouse skin tissue over 24 h. The skin temperature was maintained at 50 °C for 5 min by laser irradiation at each data point.

advantages: First, GO has a long-lasting mechanical anti-microbial effect (2–5 days shown in Figure 4 Figures S10 and S11), so GO-DPMNs can prevent microbial infections until complete healing of the insertion sites over 6–24 h.^{12,41} Unlike small antibiotic molecules or dissolved silver ions, GO does not diffuse quickly or decompose within the insertion pores in the skin tissue, enabling their long-acting effect. Second, the combined antibacterial mechanism, that is, mechanical and chemical, makes it extremely difficult for microbes to evolve GO-resistant strains because microbes must use phospholipid-based cell membranes, which are susceptible to both mechanical damage and chemical oxidation.

Photothermal GO composite DPMNs provide a simple and effective means for controlled drug release. As shown in Figure 5, because of the NIR absorbance of the GO–PVP composite (Figure 5a) and photothermal conversion (Figure 5b), the in vivo transdermal drug permeation kinetics could be controlled by shining a laser pointer ($\lambda = 850$ nm) on skin tissue embedded with DPMNs containing 500 $\mu\text{g/mL}$ GO, in contrast with PVP MNs containing 0–100 $\mu\text{g/mL}$ GO where the drug release kinetics were primarily determined by polymer dissolution kinetics and drug diffusion (Figure 5c). Moreover, the GO photothermal effect within the MN further enhances its self-sterilizing properties. For example, although the GO composite (500 $\mu\text{g/mL}$) with either CMC or HA was only able to kill 50–60% of the *E. coli* added to the MN surface, upon NIR irradiation, 93.3–98.3% bacteria were eliminated (Figure S11). Although the GO-doped composite materials have been used for photothermal therapy in cell models,¹⁹ their large size and planar morphology limits it to inefficient superficial applications because it is incapable of free migration within skin tissue. In contrast, this localized photothermal effect within the MNs enables effective photo-activatable drug release and photothermal sterilization of the MN insertion sites.

GO does not affect DPMN biocompatibility, as demonstrated by an in vitro cytotoxicity evaluation.^{12,42} As shown in Figure S12, even when exposed to 500 $\mu\text{g/mL}$ GO in cell culture medium for 24 h, the viability of human embryonic skin fibroblasts (CCC-ESFs) was insignificantly affected, with $93 \pm 4\%$ of the cells remaining viable. However, exposure to 1000 $\mu\text{g/mL}$ GO decreased the cell viability by 10–20%. Furthermore, we observed an anti-inflammatory effect by GO-doped DPMNs (Figure S13). The exposure of innate immune cells, that is, M1 macrophages, to GO–PVP DPMNs dissolved in cell culture medium significantly reduced the expression of pro-inflammatory cytokines, including tumor necrosis factor-alpha (TNF α) and two interleukins (IL-1 β and IL-6). This anti-inflammatory property, via modification of immunometabolism of cells,^{43–45} is important because it can prevent clinical issues resulting from inflammation, such as slow healing or chronic wounds.

The feasibility of the GO-doped DPMNs for transdermal drug delivery was demonstrated through the treatment of melanoma in xenograft mouse models. Melanoma tumors were grafted to BALB/c-nu/nu mice by subcutaneous injection of human melanoma cells B16F10 on their left flank. Based on the excellent performance of PVP-based DPMNs containing 500 $\mu\text{g/mL}$ GO regarding their mechanical and antibacterial properties, they were selected for the in vivo experiment. Every MN tip was loaded with 0.5 μg of HA15, an emerging anti-melanoma drug that can effectively target HSPAS/BiP, a master regulator of the unfolded protein response, to kill cancer cells by inducing autophagy and apoptosis.^{46–48}

Mice were randomly placed into five groups (6 mice/group): saline MNs (negative control), GO MNs (negative control), GO-HA15 MNs (treatment), HA15 MNs (treatment), and hypodermic injection of HA15 (“HA15 SC + laser”, positive control). To correct for any potential effect from laser irradiation, we applied the same 10 min NIR

irradiation to all five groups immediately after every treatment using an 850 nm laser. As presented in photographs and tumor growth curves (Figure 6a,b), the negative control MNs

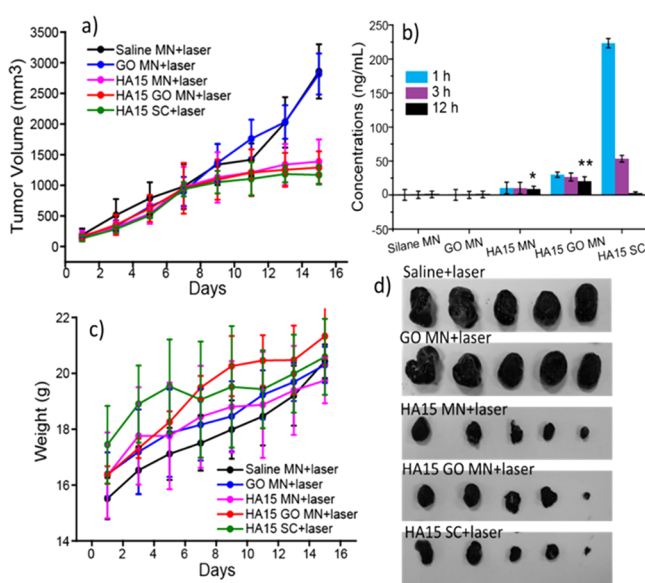


Figure 6. In vivo anticancer effect of microneedles (MNs) containing HA15 for melanoma therapy. (a) Tumor volume, (b) HA15 plasma concentration, and (c) body weight change of each treatment group over the 15 day treatment ($n = 5$). (d) Digital photos of the post-treatment tumors from each of the five groups: Negative control: saline and GO MNs; treatment group: GO-HA15 and HA15 MNs; and positive control: HA15 SC. To correct for any potential effect from laser irradiation, 10 min of laser (850 nm) irradiation was applied to every group.

containing no HA15 but only either saline or GO did not inhibit tumor growth. In contrast, the group treated with GO-HA15 MNs exhibited excellent antitumor efficacy, similar to the two positive controls that introduced HA15 with regular MNs (without GO) or hypodermic injections. However, the metabolic rates of HA15 in plasma after administration were quite different (Figure 6c). After 1 and 3 h of HA15 administration, the plasma concentrations of HA15 in the two MN groups were significantly lower than when using hypodermic injections for HA15 administration. However, after 12 h, the HA15 concentrations of the MN groups were significantly higher than that of the hypodermic injection group. In the two MN groups, the drug concentrations were stable with a slow decrease, in contrast to the sharp increase followed by the decrease of plasma drug concentrations in the hypodermic injection group. Presumably, this is because of the slow drug release and diffusion kinetics within the dermis by MN injection (the MN height is 750 μm) than under the dermis by hypodermic injection. Interestingly, we observed higher plasma drug concentration in the GO-MN group than the regular MN group at all three time points, which is likely because of the GO photothermal effect, which facilitated the MN dissolution, drug release, and drug diffusion. Taken together, this in vivo experiment demonstrates the advantages of MNs, especially GO-doped MNs, for effective skin cancer treatment by controlled drug delivery to the lesions. The photothermal effect of GO-doped MNs is a convenient approach for tuning the pharmacokinetics.

To evaluate the toxicity of the treatment to mice, first, we analyzed aspartate aminotransferase (AST) and alanine aminotransferase (ALT) levels as indicators of liver function. The results (Figure S14) showed that the GO-doped MNs did not elevate the blood AST and ALT levels, indicating no harmful effect on mouse liver function. Second, histological images of the dissected organs were obtained to evaluate pathological damage to the major organs by the GO MNs (Figure S15). Compared to the control group treated with blank PVP MNs, there was no significant damage to the major organs, including the lungs, liver, and kidneys, induced by either GO, HA15, or their combination, which further demonstrates the biocompatibility of GO MNs during melanoma treatment. Last, the body weight increase as a function of treatment time was consistent through all groups, indicating no significant adverse effect of the HA15 treatment. Overall, the results suggest the effectiveness and safety of GO-doped DPMNs for transdermal drug delivery.

3. CONCLUSIONS

In this study, a small amount of graphene oxide (GO) was directly loaded into DPMNs to improve their properties for transdermal drug delivery. GO could remarkably enhance the MN mechanic strength and moisture resistance and contributes to self-sterilization and antibacterial properties, NIR light-activated controlled drug release, and anti-inflammatory effects. GO-doped DPMNs were then applied for the treatment of melanoma-bearing mice through delivery of HA15, with high therapeutic efficacy, NIR controlled release, and safe application. Consequently, this study may facilitate the generation of novel multifunctional GO-doped DPMNs for transdermal drug delivery.

4. MATERIALS AND METHODS

4.1. Materials. Poly(vinylpyrrolidone) (PVP 30K, MW = 30,000 Da) was obtained from Sangon Biotech (Shanghai, China). Carboxymethyl cellulose (CMC, MW = 250,000 Da) and carboxymethyl cellulose (CMC, MW = 90,000 Da) were obtained from J&K Chemical Co., Ltd. (Beijing, China). Sodium hyaluronate (HA, MW = 200,000–300,000 Da) was purchased from Top Science Biological Technology Co. (Shandong, China). Graphene oxide (GO) was purchased from XFNano Material Tech Co., Ltd. (product no. XF033, Nanjing, China). 3-[4,5-Dimethylthiazol-2-yl]-2,5-diphenyltetrazolium bromide (MTT) was purchased from the Beyotime Institute of Biotechnology (Haimen, China). ELISA kits for human IL-6, TNF- α , and IL-1 β were purchased from Dakewe Biotech Co. Ltd. (Shenzhen, China). Fluorescein isothiocyanate (FITC) and lipopolysaccharides (LPSs) were purchased from Sigma-Aldrich (St. Louis, MO, USA). Phorbol 12-myristate-13-acetate (PMA) was purchased from Meilun Biotechnology Co., Ltd. (Dalian, China). HA15 was obtained from Selleck Chemicals (Houston, TX, USA). A poly(dimethylsiloxane) kit (prepolymer and cross-linker, Sylgard 184) was purchased from Dow Corning (Midland, MI, USA). *S. aureus* (ATCC 6538D-5) and *E. coli* (ATCC 8739D-5) were purchased from American Type Culture Collection (ATCC). Tryptone soy broth (TSB), Luria-Bertani broth (LBB), and the nutrient agar plates were purchased from Huankai Microbial Sci. & Tech. Co. (Guangzhou, China). The MN mold was supplied by Zhongcheng 3D Technology Co., Ltd. (Beijing, China). The human monocyte cell line U937, human embryonic skin fibroblasts CCC-ESF, and human melanoma cell line B16F10 were obtained from the China Infrastructure of Cell Line Resource (Beijing, China). Fetal bovine serum (FBS) and the cell culture medium were obtained from Invitrogen Life Technologies (Carlsbad, CA, USA). ALT and AST assay kits were obtained from Elabscience Biotechnology Co. Ltd. (Wuhan, China).

4.2. Microneedle Fabrication. In this study, we used PVP, CMC, and HA to fabricate GO-containing microneedles. In brief, 2 mg/mL GO solution was prepared by dispersing GO in deionized water with 30–60 min of sonication. Various volumes of GO solution were mixed with aqueous PVP, CMC, and HA solutions to reach final GO concentrations of 0, 10, 100, 500, and 1000 $\mu\text{g}/\text{mL}$. The solutions were sonicated for 5 min to obtain a uniform dispersion of GO in the polymer. The final concentrations of PVP, CMC, and HA were 1000, 80, and 150 mg/mL, respectively. In addition, 1000 mg of PVP was dissolved in 975 μL of ultrapure water. A stock solution of HA15 was prepared in DMSO with a concentration of 400 mg/mL. Then, 25 μL of the HA15 solution was added and dispersed uniformly in the PVP solution. Afterward, air bubbles in the solutions were removed by centrifugation at 8000 rpm for 5 min with a bench-top centrifuge.

The microneedles were cast in PDMS molds (**Scheme S1**). Briefly, the MN molds made from PDMS were treated with an O₂ plasma cleaner (Mingheng Science and Technology Development Co., Ltd., Chengdu, China) for 20 s to increase the hydrophilicity of their microvoids, which were then filled with 150 μL of polymer solution. The MNs were allowed to set at 40 °C for 12 h. Afterward, the MNs were gently peeled from the mold using adhesive tape and stored in a desiccator until further use.

4.3. Microneedle Characterization. To study the morphology of the control and GO-loaded MNs with scanning electron microscopy, first, the MN patches were broken into pieces using a grinder and scattered onto conductive tape. The samples were sputter-coated with 8 nm of platinum using a Leica SCD500 cryo sputter coater (Leica Microsystems, Vienna, Austria) for 30 s. Afterward, the MNs were imaged under a ZEISS SUPRA 55 scanning electron microscope (SEM; Carl Zeiss, Oberkochen, Germany).

The GO distribution through the PVP MNs was investigated by Raman spectroscopy. The Raman measurements were performed using a spectrometer (iHR 320, HORIBA Scientific, U.K.) coupled with an EMCCD camera (Newton, Andor, Northern Ireland). A diode laser operated at 532.1 nm that illuminated the sample through a microscope objective was used for excitation. The desired area of the sample was selected for Raman measurements under laser irradiation with a ~1 μm field of view. All spectra were baseline-corrected, averaged, and smoothed.

To obtain detailed morphological information, the MN patches were imaged with a cellphone camera assisted by a 45× handheld loupe (YIMOO, Shenzhen, China) and a ZEISS SUPRA 55 scanning electron microscope (SEM; Carl Zeiss, Oberkochen, Germany). In addition, the mechanical strengths of the MN patches with different GO concentrations (0, 10, 100, 500, and 1000 $\mu\text{g}/\text{mL}$) were measured with a universal testing machine (AI-7000S, Gotech, Taiwan). Initially, an MN patch was placed on a flat rigid surface of the base plate. The maximum loading force was set at 50.0 kN. The moving speed of the stainless steel plate toward the MN patch was 300 $\mu\text{m}/\text{min}$. The failure force was recorded when the MNs break. The data was collected every 0.0001 s to obtain the stress-strain relationship. All the tests were performed in triplicate.

4.4. In Vitro Microneedle Skin Penetration. PVP MNs with different GO concentrations (0, 10, 100, 500, and 1000 $\mu\text{g}/\text{mL}$) were applied to test their skin penetration ability. Initially, the abdominal skins of healthy Kunming strain mice (20–25 g, the Laboratory Animal Center of Southern Medical University) were isolated and washed with 75% (v/v) ethanol solution. The skins were then washed with 0.9% (v/v) NaCl solution twice. The water on the skin surface was removed using filter paper, and then the skins were fixed on glass slides for the experiment. Next, the PVP MN patches were inserted into the skins gently and vertically, and a 200 g weight was placed on the MN surface for 5 min. After removing the weight, the MN patch was left on the skin for another 10 min for complete dissolution of the MN shafts, and then the MN backside was removed. The insertion depth in the skins was determined on frozen tissue sections. Generally, the isolated skin sections were first kept in a freezer at -80 °C for 10 min, and then they were embedded in an optimum cutting temperature compound (OCT) in a cryostat mold. The frozen

samples were cut into 10 μm -thick sections using a cryotome (Leica RM 2235, Leica Microsystems Nussloch GmbH, Nussloch, Germany). The skin samples were stained with hematoxylin and eosin, and the images were taken under an inverted microscope (Leica DMI4000B, Leica Co. Ltd., Bensheim, Germany).

4.5. Microneedle Moisture Resistance. PVP and GO-PVP MN patches were placed in a culture dish containing a small amount of deionized water in an atmosphere with a relative humidity of 60%. The MN patch morphologies were recorded using a digital camera over 3 h. In addition, the mechanical strengths of PVP and GO-PVP MN samples were measured after 15 min of moisture exposure.

4.6. Antibacterial Assay. The GO-loaded PVP MN patches with final GO concentrations of 0, 10, 100, 500, and 1000 $\mu\text{g}/\text{mL}$ were applied to study their antibacterial properties. Two normal bacterial strains, that is, *S. aureus* and *E. coli*, were used because they commonly cause nosocomial infections. In detail, the selected bacterial strains were revived from a freezer at -80 °C and placed on nutrient agar plates. An isolated colony of *S. aureus* was inoculated in fresh TSB, and one of the *E. coli* was inoculated in fresh LBB. When they were grown into a mid-log phase (OD 600 nm, ~0.3 to 0.5), the bacterial suspensions were diluted to a 1 × 10⁷ colony forming unit (CFU)/mL solution using the culture media. Then, 50 μL of the diluted bacterial suspensions was added onto the surface of the MN patches. They were then dissolved in 1 mL of culture medium. The culture media were irradiated with an 850 nm NIR laser (1000 mW), and the media were maintained at 50 °C for 5 min. Next, 20 μL of the test samples was added to separate nutrient agar plates and spread uniformly with a sterile spreader. They were incubated at 37 °C for 24 h. The antibacterial activity was evaluated by counting the numbers of colonies.

In addition, the GO-loaded PVP MN patches with final GO concentrations of 0, 10, 100, 500, and 1000 $\mu\text{g}/\text{mL}$ were exposed to air for 3 days. Afterward, they were dissolved into 1 mL of LBB culture medium and incubated at 37 °C for 5 days. The mycetes were evident on the plates, and photographs were recorded using a cellphone camera.

4.7. In Vitro Transdermal Drug Delivery. FITC was chosen as a model drug for in vitro evaluation of transdermal drug delivery efficacy because of its strong fluorescence and high chemical stability in buffer. In detail, PVP solution was prepared and divided into four tubes. GO was added into the solutions to reach the final concentrations of 0, 10, 100, and 500 $\mu\text{g}/\text{mL}$. Then, FITC was added into the solutions with a final concentration of 20 mM. Finally, the MN patches were fabricated following the aforementioned process (**Scheme S1**).

The transdermal delivery of FITC was conducted by using a vertical Franz diffusion cell system (TP-6, Tianguang Photoelectric Instrument Co., Tianjin, China). The isolated mice skins were first pretreated as described above. Then, FITC-loaded microneedle patches with different GO concentrations were inserted into the skin using a 200 g weight for 5 min and left for another 10 min for dissolution. Afterward, the MN backsides were removed, and the skins were placed onto the Franz cell with the dermal side facing the receptor chamber and with the MN treatment areas at the center of the cell. The permeation area of the Franz cell was ~1.77 cm² (with a diameter of 1.5 cm). The receptor chamber was filled with PBS solution (20 mL, pH 7.4). The experiment was performed at 37 °C in a water bath incubator and with continuous stirring at 600 rpm. At each time point (2, 4, 8, 12, 16, and 24 h), 200 μL of the solution in the receptor chamber was collected and replaced with an equal volume of PBS buffer. Right after each time point, the skin was irradiated with an 850 nm near-infrared (NIR) laser light (1000 mW), and the skin temperature was maintained at 50 °C for 5 min. Afterward, 200 μL of solution was collected and replaced with an equal volume of PBS buffer at the time points 3, 5, 9, 13, 17, and 25 h. The samples collected from the Franz cells were stored at -20 °C until analysis. The amounts of FITC permeated from the MN patches were determined using a microplate reader (SpectraMax MSe, Molecular Devices, San Jose, CA, USA) with excitation and emission

at 494 and 520 nm, calibrated using a standard curve for FITC. The measurements were performed in triplicate.

4.8. In Vivo Antitumor Efficacy. All of the animal studies were performed in the laboratory animal center, Cancer Hospital, Chinese Academy of Medical Sciences, Shenzhen Center. The experimental procedures were based on the guidelines on animal care and use of Principles of Laboratory Animal Care (NIH publication no. 86-23, revised 1985) and approved by the Institutional Animal Care Committee at the Cancer Hospital, Chinese Academy of Medical Sciences, Shenzhen Center (no. NCC2019A005).

Female BALB/c-nu/nu mice (11–13 g, 21–28 days) were supplied by the Southern Medical School Laboratory Animal Center (no. 44002100020555). The mice (when their body weight reached 15–18 g) were used to evaluate the antitumor efficacy of HA15 MNs in vivo. In detail, 100 μL of 5×10^6 cells/mL B16F10 cells was subcutaneously injected into the left flank of BALB/c-nu/nu mice. When the tumor volume grew to 70–100 mm^3 , the mice were randomly divided into five groups (six mice per group): Every group was treated with NIR irradiation on the MNs using an 850 nm laser for 10 min to compensate for any NIR-induced variations: specifically, (1) the saline plus laser group where the mice were treated with saline MNs on the tumor sites before NIR irradiation; (2) the GO MNs plus laser group in which the tumors were treated with GO-loaded MNs (500 $\mu\text{g}/\text{mL}$ GO) transdermally followed by 10 min NIR irradiation; (3) the HA15 MNs plus laser group in which the mice were treated with GO-loaded MNs ~1.5 cm from the tumor sites, plus NIR irradiation; (4) the HA15 GO MNs plus laser group where the tumors were treated with HA15 and GO-loaded MNs (500 $\mu\text{g}/\text{mL}$ GO) transdermally and under NIR irradiation; and (5) the subcutaneous injection group where the mice were injected with HA15 solution (0.05 mg/mouse) followed by NIR irradiation. Each MN patch was inserted into the skin with a thumb pressing for 5 min and left in place for 20 min before removal. The mice were treated and their tumor volume and body weight were recorded every 2 days. On day 15, the mice in each group were sacrificed for further analysis.

4.9. Plasma Concentration. After 1, 3, and 12 h for each treatment group, the blood of the mice was collected directly from the eyes. The blood samples were stored at 4 °C overnight and centrifuged at 3000 rpm for 20 min to collect the plasma. The plasma was stored at -80 °C until use. Before analysis, the plasma samples were thawed to ambient temperature. Methanol (150 μL) was added to 50 μL of the plasma sample in a 1.5 mL Eppendorf tube and vortexed for 5 min for protein precipitation. After centrifuging at 12,000 rpm for 10 min, the supernatant was filtered through a 0.22 μm pore membrane and transferred to an autosampler vial. The samples were quantified using a Shimadzu HPLC system (Kyoto, Japan) equipped with an AB SCIEX QTRAP 6500 tandem mass spectrometer (AB SCIEX, Framingham, MA, USA). The chromatographic separations were achieved on an SHIM-PACK GISS C18 column (50 mm × 2.1 mm, 1.9 μm , Shimadzu, Kyoto, Japan) by gradient elution using mobile phases of (A) HPLC-grade water with 0.1% trifluoroacetic acid (TFA) and (B) HPLC-grade methanol at a flow rate of 0.3 mL/min. The gradient started with 5% B for the first 2 min, ramping to 90% B over 1 min, and held constant for 2 min before decreasing back to 5% B over 0.3 min. This resulted in a 5.3 min total run time including reconditioning of the column. The quantification of HA15 was performed using the multiple reaction monitoring (MRM) method with the mass transition of m/z 467.1 → 170.1 Da.

ASSOCIATED CONTENT

Supporting Information

The Supporting Information is available free of charge at <https://pubs.acs.org/doi/10.1021/acsami.9b19518>.

Experimental details of in vitro dissolution of FITC from PVP and GO-PVP MNs, cell culture; ELISA assay, cytotoxicity assay, and toxicity evaluation; microneedle patch fabrication process (Scheme S1); supporting data,

including SEM images of CMC and HA microneedle patches (Figures S1 and S2); mapping graphene oxide (GO) in GO-PVP MN, GO-HA MN, and GO-CMC MN patches with Raman spectroscopy (Figures S3, S4, and S5); SEM cross-sectional images of the MNs (Figure S6); mechanical strength of the GO-CMC MNs and GO-HA MNs (Figure S7); dissolution kinetics of the MNs (Figure S8); mechanical strength of the GO-doped MNs made of CMC 250 K and CMC 90 K (Figure S9); antibacterial effects of the GO-doped MNs (Figures S10 and S11); MTT assay of CCC-ESF cells treated with GO-doped MNs (Figure S12); activation response of M1 macrophages by GO-doped MNs (Figure S13); liver toxicity determination (Figure S14); and histological study (Figure S15) ([PDF](#))

AUTHOR INFORMATION

Corresponding Author

*E-mail: xu_zhang@cbu.ca.

ORCID

Tiangang Luan: [0000-0002-1546-0902](https://orcid.org/0000-0002-1546-0902)

Xu Zhang: [0000-0002-8098-0410](https://orcid.org/0000-0002-8098-0410)

Notes

The authors declare no competing financial interest.

ACKNOWLEDGMENTS

This work was supported by the Beatrice Hunter Cancer Research Institute (BHCRI) New Investigator Award, China Postdoctoral Science Foundation (2019-M653139, 2019-M653979), Guangdong Province Higher Vocational College & School's Pearl River Scholar Funded Scheme (2017), Shenzhen Science and Technology Program (GJHZ20180928161212140), Canada Research Chairs program, New Frontiers in Research Fund - Exploration (NFRFE-2018-01005), Atlantic Canada Opportunities Agency AIF program, Cape Breton University RISE program, NSERC Discovery Grants Program, and Post-doctoral Foundation Project of Shenzhen Polytechnic (6019330001K, 6019330006K, and 6019330007K).

REFERENCES

- (1) Park, J.-H.; Allen, M. G.; Prausnitz, M. R. Biodegradable Polymer Microneedles: Fabrication, Mechanics and Transdermal Drug Delivery. *J. Controlled Release* **2005**, *104*, 51–66.
- (2) Miyano, T.; Tobinaga, Y.; Kanno, T.; Matsuzaki, Y.; Takeda, H.; Wakui, M.; Hanada, K. Sugar Micro Needles as Transdermic Drug Delivery System. *Biomed. Microdevices* **2005**, *7*, 185–188.
- (3) Park, J.-H.; Allen, M. G.; Prausnitz, M. R. Polymer Microneedles for Controlled-Release Drug Delivery. *Pharm. Res.* **2006**, *23*, 1008–1019.
- (4) Lee, J. W.; Park, J.-H.; Prausnitz, M. R. Dissolving Microneedles for Transdermal Drug Delivery. *Biomaterials* **2008**, *29*, 2113–2124.
- (5) Li, W.; Terry, R. N.; Tang, J.; Feng, M. R.; Schwendeman, S. P.; Prausnitz, M. R. Rapidly Separable Microneedle Patch for the Sustained Release of a Contraceptive. *Nat. Biomed. Eng.* **2019**, *3*, 220–229.
- (6) Wang, C.; Ye, Y.; Hochu, G. M.; Sadeghifar, H.; Gu, Z. Enhanced Cancer Immunotherapy by Microneedle Patch-Assisted Delivery of Anti-PD1 Antibody. *Nano Lett.* **2016**, *16*, 2334–2340.
- (7) Ye, Y.; Yu, J.; Wen, D.; Kahkoska, A. R.; Gu, Z. Polymeric Microneedles for Transdermal Protein Delivery. *Adv. Drug Delivery Rev.* **2018**, *127*, 106–118.
- (8) Kim, N. W.; Kim, S. Y.; Lee, J. E.; Yin, Y.; Lee, J. H.; Lim, S. Y.; Kim, E. S.; Duong, H. T. T.; Kim, H. K.; Kim, S.; Kim, J. E.; Lee, D.

- S.; Kim, J.; Lee, M. S.; Lim, Y. T.; Jeong, J. H. Enhanced Cancer Vaccination by *In Situ* Nanomicelle-Generating Dissolving Microneedles. *ACS Nano* **2018**, *12*, 9702–9713.
- (9) Sullivan, S. P.; Koutsonanos, D. G.; del Pilar Martin, M.; Lee, J. W.; Zarnitsyn, V.; Choi, S.-O.; Murthy, N.; Compans, R. W.; Skountzou, I.; Prausnitz, M. R. Dissolving Polymer Microneedle Patches for Influenza Vaccination. *Nat. Med.* **2010**, *16*, 915–920.
- (10) McCrudden, M. T. C.; Alkilani, A. Z.; Courtenay, A. J.; McCrudden, C. M.; McCloskey, B.; Walker, C.; Alshraiedeh, N.; Lutton, R. E. M.; Gilmore, B. F.; Woolfson, A. D.; Donnelly, R. F. Considerations in the Sterile Manufacture of Polymeric Microneedle Arrays. *Drug Delivery Transl. Res.* **2015**, *5*, 3–14.
- (11) Donnelly, R. F.; Singh, T. R. R.; Alkilani, A. Z.; McCrudden, M. T. C.; O'Neill, S.; O'Mahony, C.; Armstrong, K.; McLoone, N.; Kole, P.; Woolfson, A. D. Hydrogel-Forming Microneedle Arrays Exhibit Antimicrobial Properties: Potential for Enhanced Patient Safety. *Int J Pharm* **2013**, *451*, 76–91.
- (12) García, L. E. G.; MacGregor, M. N.; Visalakshan, R. M.; Ninan, N.; Cavallaro, A. A.; Trinidad, A. D.; Zhao, Y.; Hayball, A. J. D.; Vasilev, K. Self-Sterilizing Antibacterial Silver-Loaded Microneedles. *Chem. Commun.* **2019**, *55*, 171–174.
- (13) McAllister, D. V.; Wang, P. M.; Davis, S. P.; Park, J.-H.; Canatella, P. J.; Allen, M. G.; Prausnitz, M. R. Microfabricated Needles for Transdermal Delivery of Macromolecules and Nanoparticles: Fabrication Methods and Transport Studies. *Proc. Natl. Acad. Sci. U.S.A.* **2003**, *100*, 13755–13760.
- (14) Chen, M. C.; Lin, Z. W.; Ling, M. H. Near-Infrared Light-Activatable Microneedle System for Treating Superficial Tumors by Combination of Chemotherapy and Photothermal Therapy. *ACS Nano* **2016**, *10*, 93–101.
- (15) Zhang, Y.; Wang, J.; Yu, J.; Wen, D.; Kahkoska, A. R.; Lu, Y.; Zhang, X.; Buse, J. B.; Gu, Z. Bioresponsive Microneedles with a Sheath Structure for H₂O₂ and pH Cascade-Triggered Insulin Delivery. *Small* **2018**, *14*, 1704181.
- (16) Justin, R.; Chen, B. Strong and Conductive Chitosan-Reduced Graphene Oxide Nanocomposites for Transdermal Drug Delivery. *J. Mater. Chem. B* **2014**, *2*, 3759–3770.
- (17) Justin, R.; Chen, B. Multifunctional Chitosan-Magnetic Graphene Quantum Dot Nanocomposites for the Release of Therapeutics from Detachable and Non-detachable Biodegradable Microneedle Arrays. *Interace Focus* **2018**, *8*, 20170055.
- (18) Justin, R.; Román, S.; Chen, D.; Tao, K.; Geng, X.; Grant, R. T.; MacNeil, S.; Sun, K.; Chen, B. Biodegradable and Conductive Chitosan-Graphene Quantum Dot Nanocomposite Microneedles for Delivery of Both Small and Large Molecular Weight Therapeutics. *RSC Adv.* **2015**, *5*, 51934–51946.
- (19) Tian, Z.; Cheng, J.; Liu, J.; Zhu, Y. Dissolving Graphene/Poly(Acrylic Acid) Microneedles for Potential Transdermal Drug Delivery and Photothermal Therapy. *J. Nanosci. Nanotechnol.* **2019**, *19*, 2453–2459.
- (20) Perreault, F.; de Faria, A. F.; Nejati, S.; Elimelech, M. Antimicrobial Properties of Graphene Oxide Nanosheets: Why Size Matters. *ACS Nano* **2015**, *9*, 7226–7236.
- (21) Lu, X.; Feng, X.; Werber, J. R.; Chu, C.; Zucker, I.; Kim, J. H.; Osuji, C. O.; Elimelech, M. Enhanced Antibacterial Activity Through the Controlled Alignment of Graphene Oxide Nanosheets. *P. Natl. Acad. Sci. USA* **2017**, *114*, E9793–E9801.
- (22) Jiang, B. P.; Zhou, B.; Lin, Z.; Liang, H.; Shen, X. C. Recent Advances in Carbon Nanomaterials for Cancer Phototherapy. *Chem-Eur. J* **2019**, *25*, 3993–4004.
- (23) Kalluru, P.; Vankayala, R.; Chiang, C.-S.; Hwang, K. C. Nano-Graphene Oxide-Mediated In Vivo Fluorescence Imaging and Bimodal Photodynamic and Photothermal Destruction of Tumors. *Biomaterials* **2016**, *95*, 1–10.
- (24) Dikin, D. A.; Stankovich, S.; Zimney, E. J.; Piner, R. D.; Dommett, G. H. B.; Evmenenko, G.; Nguyen, S. T.; Ruoff, R. S. Preparation and Characterization of Graphene Oxide Paper. *Nature* **2007**, *448*, 457–460.
- (25) Yu, X.; Cheng, H.; Zhang, M.; Zhao, Y.; Qu, L.; Shi, G. Graphene-Based Smart Materials. *Nat. Rev. Mater.* **2017**, *2*, 17046.
- (26) Chen, Y.; Gao, D.; Wang, Y.; Lin, S.; Jiang, Y. A Novel 3D Breast-Cancer-On-Chip Platform for Therapeutic Evaluation of Drug Delivery Systems. *Anal. Chim. Acta* **2018**, *1036*, 97–106.
- (27) Regehr, K. J.; Domenech, M.; Koepsel, J. T.; Carver, K. C.; Ellison-Zelski, S. J.; Murphy, W. L.; Schuler, L. A.; Alarid, E. T.; Beebe, D. J. Biological Implications of Polydimethylsiloxane-Based Microfluidic Cell Culture. *Lab Chip* **2009**, *9*, 2132–2139.
- (28) McDonald, J. C.; Whitesides, G. M. Poly(dimethylsiloxane) as a Material for Fabricating Microfluidic Devices. *Acc. Chem. Res.* **2002**, *35*, 491–499.
- (29) Young, R. J.; Kinloch, I. A.; Gong, L.; Novoselov, K. S. The Mechanics of Graphene Nanocomposites: A Review. *Compos. Sci. Technol.* **2012**, *72*, 1459–1476.
- (30) Sreenivasulu, B.; Ramji, B.; Nagaral, M. A Review on Graphene Reinforced Polymer Matrix Composites. *Mater. Today* **2018**, *5*, 2419–2428.
- (31) Zhang, W.; Guo, Z.; Huang, D.; Liu, Z.; Guo, X.; Zhong, H. Synergistic Effect of Chemo-Photothermal Therapy Using PEGylated Graphene Oxide. *Biomaterials* **2011**, *32*, 8555–8561.
- (32) Larrañeta, E.; Lutton, R. E. M.; Woolfson, A. D.; Donnelly, R. F. Microneedle Arrays as Transdermal and Intradermal Drug Delivery Systems: Materials Science, Manufacture and Commercial Development. *Mater. Sci. Eng. R* **2016**, *104*, 1–32.
- (33) Demir, Y. K.; Akan, Z.; Kerimoglu, O. Characterization of Polymeric Microneedle Arrays for Transdermal Drug Delivery. *PLoS One* **2013**, *8*, No. e77289.
- (34) Compton, O. C.; Cranford, S. W.; Putz, K. W.; An, Z.; Brinson, L. C.; Buehler, M. J.; Nguyen, S. T. Tuning the Mechanical Properties of Graphene Oxide Paper and Its Associated Polymer Nanocomposites by Controlling Cooperative Intersheet Hydrogen Bonding. *ACS Nano* **2012**, *6*, 2008–2019.
- (35) Papageorgiou, D. G.; Kinloch, I. A.; Young, R. J. Mechanical Properties of Graphene and Graphene-Based Nanocomposites. *Prog. Mater. Sci.* **2017**, *90*, 75–127.
- (36) Sausse, M.; Gobillon, C.; Lambert, P. Microneedle Array Penetration Test: Understanding the "Bed of Nails" Phenomenon. *OnDrugDelivery* **2013**, *40*, 29–32.
- (37) Yu, J.; Zhang, Y.; Ye, Y.; DiSanto, R.; Sun, W.; Ranson, D.; Ligler, F. S.; Buse, J. B.; Gu, Z. Microneedle-Array Patches Loaded with Hypoxia-Sensitive Vesicles Provide Fast Glucose-Responsive Insulin Delivery. *Proc. Natl. Acad. Sci. U.S.A.* **2015**, *112*, 8260–8265.
- (38) Chen, J.; Peng, H.; Wang, X.; Shao, F.; Yuan, Z.; Han, H. Graphene Oxide Exhibits Broad-Spectrum Antimicrobial Activity Against Bacterial Phytopathogens and Fungal Conidia by Intertwining and Membrane Perturbation. *Nanoscale* **2014**, *6*, 1879–1889.
- (39) Mangadlao, J. D.; Santos, C. M.; Felipe, M. J. L.; de Leon, A. C. C.; Rodrigues, D. F.; Advincula, R. C. On the Antibacterial Mechanism of Graphene Oxide (GO) Langmuir-Blodgett Films. *Chem. Commun.* **2015**, *51*, 2886–2889.
- (40) Hui, L.; Piao, J.-G.; Auletta, J.; Hu, K.; Zhu, Y.; Meyer, T.; Liu, H.; Yang, L. Availability of the Basal Planes of Graphene Oxide Determines Whether It Is Antibacterial. *ACS Appl. Mater. Interfaces* **2014**, *6*, 13183–13190.
- (41) Shah, V.; Choudhury, B. K. Fabrication, Physicochemical Characterization, and Performance Evaluation of Biodegradable Polymeric Microneedle Patch System for Enhanced Transcutaneous Flux of High Molecular Weight Therapeutics. *AAPS PharmSciTech* **2017**, *18*, 2936–2948.
- (42) Taheri, S.; Cavallaro, A.; Christo, S. N.; Smith, L. E.; Majewski, P.; Barton, M.; Hayball, J. D.; Vasilev, K. Substrate Independent Silver Nanoparticle based Antibacterial Coatings. *Biomaterials* **2014**, *35*, 4601–4609.
- (43) Hoyle, C.; Rivers-Auty, J.; Lemarchand, E.; Vranic, S.; Wang, E.; Buggio, M.; Rothwell, N. J.; Allan, S. M.; Kostarelos, K.; Brough, D. Small, Thin Graphene Oxide Is Anti-inflammatory Activating Nuclear Factor Erythroid 2-Related Factor 2 via Metabolic Reprogramming. *ACS Nano* **2018**, *12*, 11949–11962.

- (44) Feito, M. J.; Vila, M.; Matesanz, M. C.; Linares, J.; Gonçalves, G.; Marques, P. A. A. P.; Vallet-Regí, M.; Rojo, J. M.; Portolés, M. T. In vitro Evaluation of Graphene Oxide Nanosheets on Immune Function. *J. Colloid Interface Sci.* **2014**, *432*, 221–228.
- (45) Song, Q.; Jiang, Z.; Li, N.; Liu, P.; Liu, L.; Tang, M.; Cheng, G. Anti-Inflammatory Effects of Three-Dimensional Graphene Foams Cultured with Microglial Cells. *Biomaterials* **2014**, *35*, 6930–6940.
- (46) Cerezo, M.; Rocchi, S. New Anti-Cancer Molecules Targeting HSPA5/BIP to Induce Endoplasmic Reticulum Stress, Autophagy and Apoptosis. *Autophagy* **2016**, *13*, 216–217.
- (47) Cerezo, M.; Lehraiki, A.; Millet, A.; Rouaud, F.; Plaisant, M.; Jaune, E.; Botton, T.; Ronco, C.; Abbe, P.; Amdouni, H.; Passeron, T.; Hofman, V.; Mograbi, B.; Dabert-Gay, A.-S.; Debayle, D.; Alcor, D.; Rabhi, N.; Annicotte, J. S.; Heliot, L.; Gonzalez-Pisfil, M.; Robert, C.; Moréra, S.; Vigouroux, A.; Gual, P.; Ali, M. M. U.; Bertolotto, C.; Hofman, P.; Ballotti, R.; Benhida, R.; Rocchi, S. Compounds Triggering ER Stress Exert Anti-Melanoma Effects and Overcome BRAF Inhibitor Resistance. *Cancer Cell.* **2016**, *29*, 805–819.
- (48) Ruggiero, C.; Doghman-Bouguerra, M.; Ronco, C.; Benhida, R.; Rocchi, S.; Lalli, E. The GRP78/BiP Inhibitor HA15 Synergizes with Mitotane Action Against Adrenocortical Carcinoma Cells Through Convergent Activation of ER Stress Pathways. *Mol. Cell. Endocrinol.* **2018**, *474*, 57–64.